Pressure reconstruction from Lagrangian particle tracking with FFT integration

F. Huhn[*], D. Schanz, S. Gesemann, P. Manovski, A. Schröder

Dept. of Experimental Methods, Institute of Aerodynamics and Flow Technology, German Aerospace Center (DLR), Göttingen, Germany.

* Correspondent author: florian.huhn@dlr.de

Keywords: Lagrangian particle tracking, volumetric pressure reconstruction, helium-filled soap bubbles, LED illumination

ABSTRACT

Volumetric time-resolved pressure gradient fields in unsteady flows can be estimated through flow measurements of the material acceleration in the fluid and the assumption of the governing momentum equation. In order to derive pressure, almost exclusively two numerical methods have been used to spatially integrate the pressure gradient until now: first, direct path integration in the spatial domain, and second, the solution of the Poisson equation with numerical methods. We propose an alternative method by integrating the pressure gradient field directly in Fourier space with a standard FFT function. The method is fast and easy to implement. We demonstrate the accuracy of the integration scheme on a synthetic pressure field and apply it to an experimental example based on acceleration data from Lagrangian particle tracking with high seeding density (*Shake-The-Box* method).

An extended version of this manuscript is under consideration for publication in the peer-reviewed journal *Experiments in Fluids.*

1. Introduction

The pressure field in a turbulent flow reveals important coherent structures, e.g., vortex cores, and it is most relevant to determine the loads exerted by the fluid on a structure in the flow, e.g., a wing. Yet, spatially well resolved pressure fields $P(\mathbf{x}, t)$ in three-dimensional unsteady flows are difficult to measure. Optical, non-intrusive flow measurement techniques, in particular novel Lagrangian particle tracking approaches [Schanz et al. (2013a), Schanz et al. (2016)], can provide accurate and dense fields of the material acceleration in the fluid. The pressure gradient field $\boldsymbol{\nabla} P(x, t)$ is then derived from the Navier-Stokes equation for incompressible isothermal fluid and it is integrated in space.

For this spatial integration, almost exclusively two methods have been used in the aerodynamic and hydrodynamic flow measurement community [van Oudheusden (2013)]: first, the direct numerical integration of $\boldsymbol{\nabla} P(x, t)$ along various paths in space with some spatial marching scheme based on finite differences,

$$P(\mathbf{x} + \Delta\mathbf{x}) = P(\mathbf{x}) + \boldsymbol{\nabla} P \Delta\mathbf{x}, \tag{1}$$

and second, the numerical iterative solution of the Poisson equation,

$$\Delta P = \nabla \cdot (\nabla P) \qquad (2)$$

obtained by applying the divergence operator on the Navier-Stokes equation. The necessary Dirichlet or Neumann boundary conditions for (2) are determined from assumed flow conditions at the boundary or directly from the measured data set. Examples in which the first method was used include the experimental studies by Liu & Katz (2006), Dabiri et al. (2014), and Tronchin et al. (2015); the second method has been applied, e.g., by Ghaemi et al. (2012), Ragni et al. (2012), Novara & Scarano (2013), Pröbsting et al. (2013) and Neeteson & Rival (2015).

The problem of reconstructing a two- or three-dimensional scalar field from its spatial gradient field, however, has been considered in several other scientific fields. In computer vision, Frankot & Chellappa (1988) were the first to propose a fast method to integrate the surface gradient of a three-dimensional body, obtained from images with the 'shape from shading' visualization technique. Their method enforces integrability and integrates the gradient field in Fourier space. Without referring to the former reference, Zhang (1996) introduces the same method to reconstruct water surface elevations from optical surface slope measurements. He additionally considers the treatment of boundary effects in non-periodic domains. Both works consider two-dimensional problems, but the extension of the method to three dimensions is straightforward, as will be shown in the following. Surprisingly, this non-iterative integration technique in Fourier space has not been considered for pressure reconstruction in the aerodynamics community, so far. To the best knowledge of the authors, exclusively one group in medical imaging applies this fast integration technique to fluid flows [Wang & Amini (2005), Negahdar et al. (2013)]. They determine pressure gradient fields in blood flows, experimentally measured with magnetic resonance imaging, in order to obtain the pressure load on blood vessels. As a matter of low Reynolds numbers, the complexity of the investigated blood flow is rather low, while we will consider complex turbulent flows here.

The aim of the present paper is to present the efficient integration method for spatial gradient fields and to show its applicability to 3D time-resolved pressure fields in turbulent flows. The gradient field data we use is based on accurate material acceleration fields that have become available recently through the advent of the high-density Lagrangian particle tracking (LPT) algorithm *Shake-The-Box* [Schanz et al. (2016)] in combination with the interpolation scheme *FlowFit* [Gesemann (2015)].

The paper is organized as follows. In Sec. 2, we recall the principles of pressure reconstruction from flow measurements and present the integration method of the pressure gradient. In Sec. 3, we show examples of pressure reconstruction for a synthetic pressure field to validate the integration method, and in Sec. 4, we reconstruct the pressure field in an experimental turbulent flow. Finally, Sec. 5 summarizes the results.

2. Data and Methods

2.1 Momentum equation

The momentum $\rho\mathbf{u}$ of a fluid parcel in an isothermal viscid Newtonian fluid evolves according to the Navier-Stokes equation

$$\rho\frac{D\mathbf{u}}{Dt} = \rho\left(\frac{\partial\mathbf{u}}{\partial t} + (\mathbf{u}\cdot\boldsymbol{\nabla})\mathbf{u}\right) = -\boldsymbol{\nabla}P + \mu\Delta\mathbf{u} \tag{3}$$

with constant density ρ, constant viscosity μ, and the material acceleration $D\mathbf{u}/Dt$, i.e., the acceleration of a fluid parcel along its trajectory. Far from boundaries, the pressure gradient force typically dominates,

$$\boldsymbol{\nabla}P \gg \mu\Delta\mathbf{u}, \tag{4}$$

such that for flows with high Reynolds number, the viscous term is small and a good estimate of the pressure gradient field can be obtained by

$$\boldsymbol{\nabla}P = -\rho\frac{D\mathbf{u}}{DT} = -\rho\mathbf{a} \tag{5}$$

where we denote the material (or Lagrangian) acceleration with $\mathbf{a}$ from here on.

2.1 Measurement of Lagrangian acceleration

According to the term in brackets in Eq. (3), acceleration could simply be obtained from time-resolved velocity fields as measured with particle image velocimetry (PIV). PIV is a robust method to obtain time-resolved velocity fields from pairs of particle images. However, this indirect acceleration measurement involves spatial and temporal derivatives of the velocity field (3). The derivatives enhance measurement noise in the velocity field, which can lead to noisy acceleration fields, and consequently to noisy pressure gradient fields. Additionally, the spatial smoothing effect of the correlation window in the PIV technique may lead to an underestimation of the velocity gradient, and thus of the acceleration.

Lagrangian particle tracking (LPT) overcomes these problems by tracking individual tracer particles, such that entire time-resolved trajectories of particles $\mathbf{x}_p(\mathbf{x_0}, t_0, t)$ can be measured. Velocity and acceleration are determined as point measurements at the well-defined position of an individual tracer. Acceleration at particle positions is obtained as $\mathbf{a}(\mathbf{x_p}, t) = d^2\mathbf{x_p}(t)/dt^2$. The

main source of error influencing the acceleration value is the uncertainty of the particle position, while no spatial smoothing is involved in the image processing.

LPT has long been used in statistical turbulence research at relatively low seeding densities [see e.g., Hoyer et al. (2005) or Xu et al. (2007)]. Higher resolution has been reached by applying LPT to tomographic PIV data as a postprocessing step in order to increase the accuracy of acceleration measurements [Schröder et al. (2011)] and to reconstruct pressure fields [Novara et al. (2013)]. Only recently, the processable seeding densities in the particle images of direct LPT, measured in units of particles per pixel (ppp), increased substantially to values as large as 0.1 ppp [Schanz et al. (2014)]. Assuming a camera with a 1 Mpixel sensor, 0.1 ppp ideally corresponds to 10^5 simultaneously tracked particles, or an unstructured grid of roughly 50×50×50 positions with accurate acceleration data. This spatially resolved acceleration field allows for a LPT-based pressure reconstruction in unsteady turbulent flows.

Here, we use the LPT algorithm *Shake-The-Box* by Schanz et al. (2016). The strength of this algorithm is to use the temporal information of already established particle trajectories to predict the particle position in the next time frame and identify the corresponding intensity peak in the camera images. The predicted particle position is then reprojected to the cameras using an estimated optical transfer function (OTF) and the particle position is corrected to optimally fit the intensity peaks in the camera images. Given the optimal particle position, the intensity signature of the particle in the camera images is subtracted from the images (iterative particle reconstruction, IPR [Wieneke (2013)], in order to reduce the complexity of the particle positioning problem. This procedure is crucial to handle high seeding densities. Consecutive particle positions $\mathbf{x}_p(t)$ of an individual trajectory are fit with a continuous B-spline curve that allows to evaluate the particle position, as well as the velocity and the acceleration at any time instant of the trajectory [TrackFit, Gesemann (2015)].

In a subsequent step, the acceleration data is interpolated to a Cartesian grid with the FlowFit interpolation scheme [FlowFit, Gesemann (2015)]. Smoothing B-splines are fit iteratively to the scattered acceleration data. The B-splines are defined on a fine auxiliary grid with a selectable mean resolution given in particles per cell (ppc) with typicall values of 0.1ppc. The interpolant is smoothed by penalizing high frequencies in cells containing particles and in empty cells. Additionally, the curl of the acceleration field is penalized and tends to zero which supports integrability. Finally, the interpolant is evaluated on the output grid with a user defined spatial resolution. A high spatial sampling resolution is beneficial for the Fourier transform in the pressure integration scheme below.

2.2 Integration scheme for pressure reconstruction

Following Frankot & Chellappa (1988), we obtain the pressure field $P(\mathbf{x})$ by integrating the measured three-dimensional pressure gradient fields

$$\partial_x P = -\rho \mathbf{a_x} \tag{6}$$
$$\partial_y P = -\rho \mathbf{a_y} \tag{7}$$
$$\partial_z P = -\rho \mathbf{a_z} \tag{8}$$

in Fourier space

$$\tilde{P} = \frac{\mathbf{k}\,\widetilde{\nabla P}}{i|\mathbf{k}|^2} = \frac{k_x\,\widetilde{\partial_x P} + k_y\,\widetilde{\partial_y P} + k_z\,\widetilde{\partial_z P}}{i(k_x^2 + k_y^2 + k_z^2)} \tag{9}$$

and by transforming back to normal space

$$P'(\mathbf{x}) = FT^{-1}\tilde{P}(\mathbf{k}). \tag{10}$$

For a short derivation of (9), see Ref. [Rocholz (2008)]. The tilde denotes a Fourier transformed function, e.g., $\tilde{P}_x = FT(P_x)$, FT^{-1} is the inverse Fourier transform, and k_x, k_y, k_z are the components of the wave number vector $\mathbf{k}$. In (9), the separation of the curl-free longitudinal component of the vector field corresponds to a projection of the pressure gradient onto the k-vector $\mathbf{k}[\mathbf{k} \cdot \widetilde{\nabla P}]/|\mathbf{k}|^2$, and the integration in space corresponds to a division by $i\mathbf{k}$.

Equation (9) has a singularity at $\mathbf{k} = \mathbf{0}$. In order to handle this, the amplitude for the constant component is set to zero, $\tilde{P}(\mathbf{k} = \mathbf{0}) = 0$. By this operation, the amplitudes of the constant component of the three pressure gradients is lost. Below, we set boundary conditions at the periodic domain that account for the global linear pressure gradient.

Finally, in order to obtain total pressure, the integration constant, a constant pressure offset P_0, obtained from additional measurements or from theoretical considerations at the boundaries, is added to the relative pressure field $P(\mathbf{x})$.

2.3 Boundary conditions for periodic domain

The Fourier transform assumes an infinite periodic domain for the transformed fields, a condition that is typically not met by measurement data. A continuous extension of the field by mirroring the data has been proposed to minimize boundary artifacts due to non-periodicity of the data [Zhang (1996), Wang & Amini (2005)]. In the following, we discuss this approach and

propose a new treatment of the boundaries that suppresses boundary artifacts. The different discussed boundary conditions are depicted in Fig. 1.
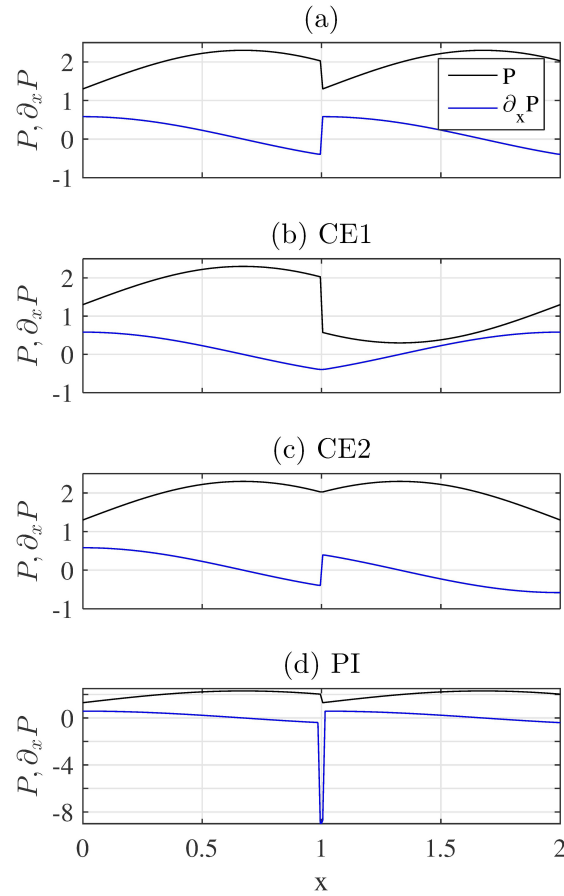
Fig. 1 Sketch of the different modified boundary conditions for the non-periodic pressure field P and pressure gradient field $\partial_x P$ (two periods of an arbitrary function are shown here for demonstration purposes). (a) Two periods of discontinuous data with period L=1. (b) Continuous extension of $\partial_x P$ (blue) by mirroring, CE1, [Zhang (1996)]. (c) Continuous extension of P (black) by mirroring, CE2, [Wang & Amini (2005)]. (d) Representation of the discontinuity in pressure with an impulsive pressure gradient obtained from path integration, PI.

Continuous extension (CE). A periodic continuous extension avoids discontinuities at the boundaries of the field subject to the FT by reflecting the field about mirror planes along the boundaries. In Eq. (9) and (10), the Fourier transform acts on the pressure gradient field and on the pressure field. A crucial point is whether to construct continuous boundaries for ∇P or for P. Zhang (1996) proposes to continuously extend ∇P by reflecting it about the axes of the coordinate system such that

$$\nabla P(\mathrm{x}, \mathrm{y}) = \nabla P(-\mathrm{x}, \mathrm{y}) = \nabla P(\mathrm{x}, -\mathrm{y}) = \nabla P(-\mathrm{x}, -\mathrm{y}). \tag{11}$$

We denote this choice of boundary conditions with a continuous extension of the gradient field as CE1. If this continuous gradient field is integrated in space, however, the resulting pressure field is not continuous at the boundaries (Fig. 1b).

Wang & Amini (2005) enforce continuity of the resulting pressure field P instead (Fig. 1c), by extending the gradient field in a discontinuous way as

$$\partial_x P(\mathrm{x,y}) = -\partial_x P(-\mathrm{x,y}) = +\partial_x P(\mathrm{x},-\mathrm{y}) = -\partial_x P(-\mathrm{x},-\mathrm{y}), \qquad (12)$$
$$\partial_y P(\mathrm{x,y}) = +\partial_y P(-\mathrm{x,y}) = -\partial_y P(\mathrm{x},-\mathrm{y}) = -\partial_y P(-\mathrm{x},-\mathrm{y}), \qquad (13)$$

where the only difference to (16) is in the signs. These boundary conditions are denoted as CE2. In numerical experiments with a synthetic multiscale pressure field (cf. Fig. 2), we find that the CE2 approach produces smaller residuals for the reconstructed pressure field than the CE1 approach.

Boundary gradients from direct path integration (PI). A disadvantage of the periodic continuous extension of the pressure field is the obvious increase of the domain size and the corresponding increase of required memory space by a factor of 8 in three dimensions due to the mirrored fields. Another way to match the boundary of the non-periodic pressure field to the periodic FFT computations is to consistently represent the high gradient of the pressure discontinuity in the gradient field (Fig. 1d). Assume a periodically extended pressure field with a discontinuity at the boundaries. The gradient of this field has high values at the boundary, which are missing in the measured gradient data. The discontinuity in the pressure field can be accounted for by an impulse at the boundary of the gradient field. The magnitude of the impulse is obtained by a direct path integration from boundary to boundary in the gradient field. Along a one-dimensional line in x-direction in the gradient field with length n, the value of the boundary impulse can be expressed as

$$\partial_x P(1) = \partial_x P(n) = -\frac{1}{2}\sum_{i=2}^{n-1} \partial_x P(i) \qquad (14)$$

The boundary values in the measured $\partial_x P$ data is then replaced by the values from Eq. (14). $\partial_y P$ and $\partial_z P$ are corrected in the same way. This modification of the boundaries is denoted as PI. After this correction of the boundaries, the gradient field line-wise satisfies

$$\int_0^L \partial_x P(x)dx = 0, \qquad (15)$$

also in y-direction and z-direction, which is equivalent with P being periodic with period L. The continuous extension approach CE2 also satisfies Eq. (16), while the approach CE1 does not.

2.4 Steps of the pressure reconstruction algorithm

Including the LPT measurement, we summarize the pressure reconstruction with the following steps:

1. Reconstruct particle trajectories from time-resolved particle images of at least three cameras using the STB algorithm [Schanz et al. (2016)].

2. Fit an interpolating continuous function consisting of 1D cubic B-splines to the trajectories and differentiate twice w.r.t. time to obtain the material acceleration at particle positions (*TrackFit*, Gesemann (2015)).

3. Interpolate the acceleration, given on an unstructured grid, to a fine Cartesian grid, using 3D cubic B-splines and penalyzing the curl of the acceleration field (*FlowFit*, Gesemann (2015)).

4. Neglect the viscous term in (3), assume constant density ρ and compute ∇P (6-8).

5. Modify ∇P by applying the CE or PI method for periodic spatial boundary conditions from Sec.2.3, in order to avoid boundary artifacts.

6. Compute the Fourier transforms of ∇P, evaluate (9), set $\tilde{P}(\mathbf{k} = \mathbf{0}) = 0$, and transform back, using a Fast-Fourier-Transform (FFT) function.

7. Add a constant pressure offset P_0 to obtain total pressure.

Regardless of the exact way to obtain the pressure gradient on a Cartesian grid, be it a different measurement technique or the additional consideration of theoretical models, e.g., a compressible flow with varying density, the integration method is anyhow applicable, starting from step 5.

3. Synthetic pressure field

In order to validate the accuracy of the integration method, we create a three-dimensional synthetic pressure field on a cubic 257×257×257 domain as ground truth data, compute the spatial gradient and reconstruct the pressure field. A direct comparison of the original and the reconstructed pressure field reveals the accuracy of the integration. In order to generate the synthetic pressure field, uniformly distributed noise in Fourier space is multiplied with a normalized correlation kernel of the form $f(\mathbf{k}) = \exp\left(-\alpha|k|^{\frac{1}{2}}\right)$. The slow decay of the kernel with an exponent 1/2 generates a wide range of scales, since turbulent pressure fields typically include large scale gradients as well as small scale structures related to vortices. When the parameter α is increased, high wavenumbers are damped and the synthetic pressure field shows larger spatial structures. For the test case shown, the parameter is set to $\alpha = 6.7$, resulting in a spatial structure of the pressure field as shown in Fig. 2a (central x-y plane).

The gradient of the periodic pressure field is computed in Fourier space by multiplying with i**k**, then, a non-periodic 100×100×100 subdomain is cropped in real space for the test. Pressure is reconstructed from the gradient fields, with and without accounting for periodic boundary conditions. With unchanged boundaries, i.e. non-periodic boundaries, the reconstructed pressure field significantly deviates from the original field (not shown). When the gradient field is continuously extended according to CE1 boundary conditions (11), the deviation is still large. Figure 2b shows the difference between original and reconstructed pressure field. In contrast, when the boundaries are modified according to the CE2 method (12-13) or the PI method (14), the reconstructed pressure field agrees with the original field within an error of less than 1%. Figures 2c and 2d show the small difference between original and reconstructed pressure field, profiles along a section in x-direction (dashed line) show the small relative error (Fig. 2e and 2f).
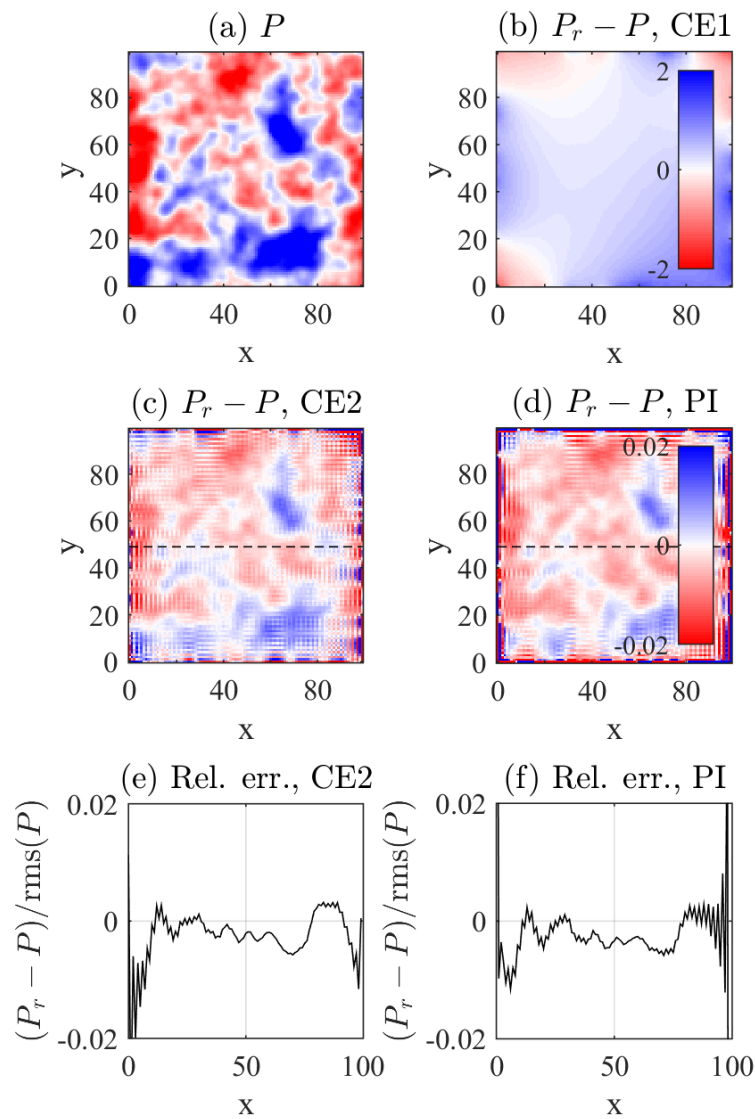
Fig. 2 (a) Synthetic three-dimensional pressure field (central plane) constructed as correlated noise. (b-d) Difference fields between reconstructed pressure field P_r and ground truth data P for different boundary conditions. Same colorbar for (a,b) and (c,d). (e,f) Relative error along a section (dashed line) for CE2 and PI boundary conditions.

Noise, always present in measurement data, is added to the synthetic pressure gradient fields to assess the effect of noise on the accuracy of the pressure field. Noise fields are created in the same way as the pressure field, i.e., as correlated noise with a correlation kernel in Fourier space $f(\mathbf{k}) = \exp(-\alpha|k|^{\frac{1}{2}})$. Fig. 3 exemplarily shows the clean pressure gradient field $\partial_x P$ together with the most extreme tested added noise field.
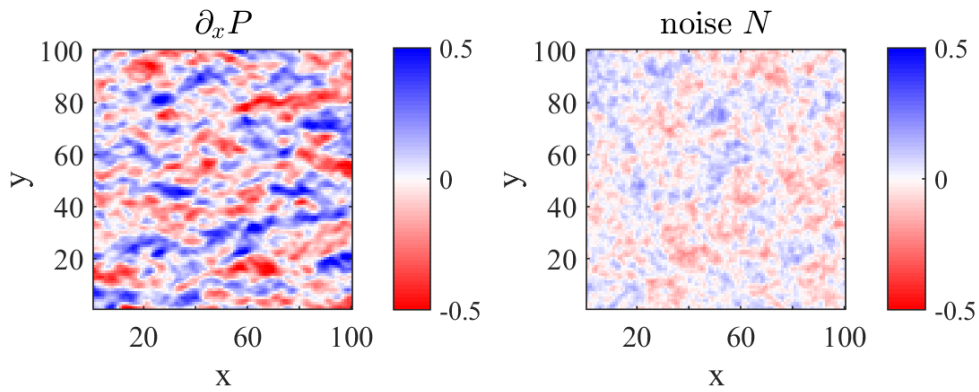
Fig. 3 (a) Clean synthetic pressure gradient field $\partial_x P$ and (b) added noise field with largest tested spatial scale parameter $\alpha = 3.3$ and largest tested relative noise amplitude $\sigma_{noise}/\sigma_P = 0.4$.

The amplitude and the spatial scale of the added noise are varied and the residual between reconstructed and original pressure field are analyzed. For PI boundary conditions, the boundary voxels in the reconstructed pressure field is typically strongly biased (Fig. 2c) due to the imposed boundary condition, and is therefore neglected in the computation of the error. Figure 4 shows the expected behavior that the error in the reconstructed pressure fields increases monotonically with increasing noise added to the pressure gradient field. In the most extreme case (large amplitude and large spatial scale of the noise, cf. Fig. 3), the added noise leads to 100% error of the reconstructed pressure field, i.e., drastically distorts the reconstructed pressure field. For moderate noise, the residual linearly decreases, converging to the error of < 1% for the noise free case. The spatial scale of the added noise has a clear influence on the resulting error of the reconstructed pressure field. At the same relative noise amplitude, the error increases with increasing spatial scale of the noise. This is expected, since the integration (division by i$\mathbf{k}$) damps small spatial scales more than large spatial scales. Overall, the two most promising boundary conditions (PI and CE2) perform equally well, with a tendency of the CE2 boundary conditions

to cause slightly smaller errors in the reconstructed pressure field, at the cost of a eight times higher data volume (mirrored field) that has to be processed.
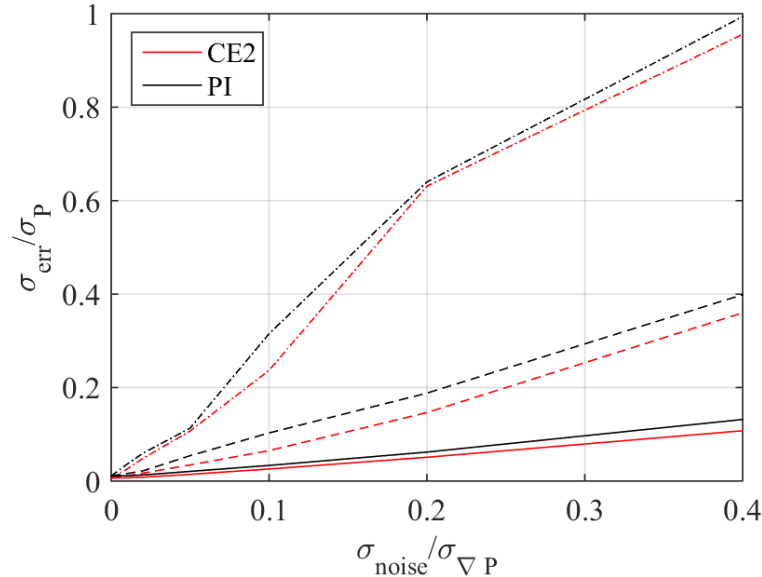

Fig. 4 Relative residual between original and reconstructed pressure field $\sigma_{err}/\sigma_P = rms(P_r - P)/rms(P)$ depending on added noise with relative amplitude σ_{noise}/σ_P and spatial scale parameter $\alpha = 1.1$ (solid line), $\alpha = 1.7$ (dashed line) and $\alpha = 3.3$ (dash-dotted line).

4. Experimental pressure field - Impinging jet

The presented integration method for the pressure gradient field is applied to an experimental data set. In the experiment, an air jet generated by a fan (PHYWE - 02742-93, upper and lower screen removed) with a nozzle exit diameter of $D = 11$cm and an exit velocity of $U \sim 5$m/s hits a flat acrylic glass plate at a distance of $H = 55$cm, $H/D = 5$, and at an angle of $\theta = 90°$. In the large measurement volume adjacent to the wall ($450×500×150$mm^3) the flow is seeded with ~180,000 helium-filled soap bubbles (HFSB) with a diameter of ~ 400μm (LaVision HFSB generator) and a mean particle distance of $d = 6.8$mm. Six high-speed cameras (PCO dimax, $2016×2016$ pix^2) record particle images at a frame rate of $f = 1$kHz at full frame size with exposure time of 130μs. The six cameras are positioned in an in-line configuration and oriented in a way that lines of sight are tangential to the flat plate. The HFSBs are illuminated by a pulsed LED array driven at 1kHz with a voltage of 44V, a current of 90A, and a pulse width of $\Delta t = 100$μs (10% duty cycle).

For the pressure reconstruction, we follow the steps outlined in Sec. 2.4. The output of the Shake-The-Box LPT algorithm provides time-resolved acceleration fields at instantaneous particle positions (Step 2). Figure 5a shows the acceleration data close to the stagnation point of the impinging jet at $(x, y) = (0,0)$. Particles are color-coded with the horizontal component of acceleration a_x with a maximal magnitude of $\sim 150 \mathrm{m/s^2}$. For the interpolation of the scattered acceleration data to a Cartesian grid with FlowFit (Step 3), the domain is extended with an empty buffer zone reaching 0.01m beyond the wall. Fig. 5b shows the interpolated acceleration field. In step 4, we set the density to $\rho = 1.2\ \mathrm{kg/m^3}$ and compute the pressure gradient ∇P. In step 5, PI boundary conditions are chosen for the FFT integration of the pressure gradient field. In step 6, the relative pressure field is obtained by integrating in Fourier space (Fig. 5c). The relative pressure field is shifted by a pressure offset such that the mean over pressure is zero in the quiescent domain $(0.2, -0.18, -0.05)\mathrm{m} < (x, y, z) < (0.3, -0.10, +0.05)\mathrm{m}$.
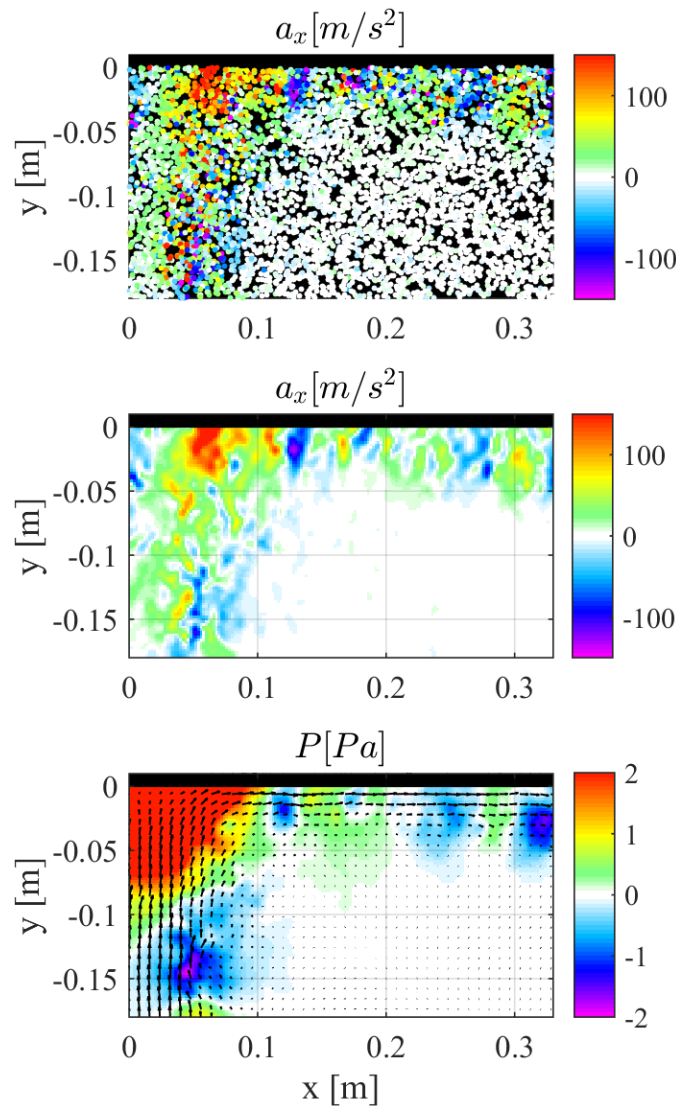
Fig. 5 (a) Particles color-coded with horizontal acceleration a_x in a slice -10mm<z<10mm. (b) Interpolation of acceleration field to Cartesian grid with FlowFit on the central z-plane. (c) Instantaneous pressure field P [Pa] and velocity field in the jet impinging onto the wall (black). Central z-plane. Maximal velocities in the domain are 4.5m/s .

The center of the jet nozzle is located outside of the presented domain at $(x, y) = (0, -55)$. Due to the swirling motion of the fan and shear instabilities, localized pressure fluctuations associated with vortices are already present in the shear layer of the jet, e.g., at $(x, y) = (0.05, -0.15)$, before the jet hits the wall These structures interact with the wall and generate new structures that are advected in positive x-direction and lead to strong pressure fluctuations at the wall.

5. Summary

Accurate and dense measurements of the material acceleration have recently become possible with the *Shake-The-Box* Lagrangian particle tracking scheme [Schanz et al. 2016]. The resulting acceleration fields are an ideal basis for a time-resolved three-dimensional reconstruction of the pressure field.

In this paper, we propose a method for the spatial integration of the pressure gradient field in turbulent flows and show the application to synthetic and experimental flow fields. The pressure gradient field is integrated in Fourier space using FFT functions that are fast and easy to implement. Before integration, the boundaries of raw data have to be modified to adjust to the periodic boundary conditions of the Fourier transform. We present two choices of periodic boundary conditions that result in numerical errors of less than 1% in the test cases shown.

6. Acknowledgments

The authors would like to thank Roland Rocholz for drawing the authors' attention to the presented integration scheme with his PhD thesis [Rocholz (2008)].

7. References

Dabiri J, Bose S, Gemell BJ, Colin SP, Costello JH (2014) An algorithm to estimate unsteady and quasi-steady pressure fields from velocity field measurements. J. Exp. Biol. 217, 331--336.

Frankot RT, Chellappa R (1988) A Method for Enforcing Integrability in Shape from Shading Algorithms. IEEE Transactions on Pattern Analysis and Machine Inteligence 10:4.

Gesemann S (2015) From particle tracks to velocity and acceleration fields using B-splines and penalties. arXiv:1510.09034v1.

Ghaemi S, Ragni D, Scarano F (2012) PIV-based pressure fluctuations in the turbulent boundary layer. Exp. Fluids 53:1823–1840.

Griffiths, D (1999) Introduction to Electrodynamics, Prentice Hall, Upper Saddle River, New Jersey, p. 555-557.

Hoyer K, Holzner M, Lüthi B, Guala M, Liberzon A, Kinzelbach W (2005) 3D scanning particle tracking velocimetry. Exp. Fluids 39, 923--934.

Liu X, Katz J. (2006) Instantaneous pressure and material acceleration measurements using a four-exposure PIV system. Exp. Fluids 41, 227–240.

Negahdar MJ, Kadbi M, Cha J, Cebral J, Amini A (2013) Noninvasive 3D Pressure Calculation From PC-MRI Via Non-Iterative Harmonics-based Orthogonal Projection: Constant Flow Experiment. 35th Ann. Int. Conf. IEEE EMBS, Osaka, Japan.

Neeteson, NJ, Rival DE (2015) Pressure-field extraction on unstructured flow data using a Voronoi-tesselation-based networking algorithm: a proof-of-principle study. Exp. Fluids 56:44.

Novara M, Scarano F. (2013) A particle-tracking approach for accurate material derivative measurements with tomographic PIV. Exp. Fluids 54:1584.

van Oudheusden BW (2013) PIV-based pressure measurement. Meas. Sci. Technol. 24, 032001.

Pröbsting S, Scarano F, Bernardini M, Pirozolli S (2013) On the estimation of wall pressure coherence using time-resolved tomographic PIV. Exp. Fluids 54:1567.

Ragni D, van Oudheusden BW, Scarano F (2012) 3D pressure imaging of an aircraft propeller blade-tip flow by phase-locked stereoscopic PIV. Exp. Fluids 52:463–477.

Rocholz, R (2008) Spatio-Temporal Measurement of Short Wind-Driven Water Waves. Dissertation, Ruperto-Carola University of Heidelberg, Germany, 2008.

Schanz D, Schröder A, Gesemann S, Michaelis D, Wieneke B (2013a) 'Shake The Box': A highly efficient and accurate Tomographic Particle Tracking Velocimetry (TOMO-PTV) method using prediction of particle positions. 10th Int. Symp. on Part. Imag. Vel., Delft, Netherlands.

Schanz D, Schröder A, Gesemann S (2014) 'Shake The Box' - a 4D PTV algorithm: Accurate and ghostless reconstruction of Lagrangian tracks in densely seeded flows. 17th Int. Symp. Appl. Laser Tech. Fluid Mech., Lisbon.

Schanz D, Gesemann S, Schröder A (2016) Shake-The-Box: Accurate Lagrangian particle tracking at high particle densities. Exp. Fluids 57:70.

Schröder A, Geisler R, Staack K, Elsinga GE, Scarano F, Wieneke B, Henning A, Poelma C, Westerweel J (2011) Eulerian and Lagrangian views of a turbulent boundary layer flow using time-resolved tomographic PIV. Exp. Fluids 50, 1071-1091.

Tronchin T, David L, Farcy A (2015) Loads and pressure evaluation of the flow around a flapping wing from instantaneous 3D velocity measurements. Exp. Fluids 56:7.

Wang Y, Amini A (2005) Integrable pressure gradients via harmonics-based orthogonal projection. In: Christensen GE, Sonka M (Eds.) Information Processing in Medical Imaging 2005, LNCS 3565, pp. 431--442, Springer-Verlag, Berlin Heidelberg.

Wieneke B (2013) Iterative reconstruction of volumetric particle distribution. Meas. Science Tech. 24, 024008.

Xu H, Oullette N, Vincenzi D, Bodenschatz E (2007) Acceleration Correlations and Pressure Structure Functions in High-Reynolds Number Turbulence. Phys. Rev. Lett. 99, 204501.

Zhang X (1996) An Algorithm for calculating water surface elevations from surface gradient data. Exp. Fluids 21, 43--48.